Secondary flows in a laterally heated horizontal cylinder

Isabel Mercader, Odalys Sánchez, and Oriol Batiste

Citation: Physics of Fluids (1994-present) **26**, 014104 (2014); doi: 10.1063/1.4856615
View online: http://dx.doi.org/10.1063/1.4856615
View Table of Contents: http://scitation.aip.org/content/aip/journal/pof2/26/1?ver=pdfcov
Published by the AIP Publishing

PHYSICS OF FLUIDS **26**, 014104 (2014)

Secondary flows in a laterally heated horizontal cylinder

Isabel Mercader,[a] Odalys Sánchez,[b] and Oriol Batiste[c]
Departament de Física Aplicada, Universitat Politècnica de Catalunya, Mòdul B4, 08034 Barcelona, Spain

(Received 11 June 2013; accepted 10 December 2013; published online 8 January 2014)

In this paper we study the problem of thermal convection in a laterally heated, finite, horizontal cylinder. We consider cylinders of moderate aspect ratio (height/diameter ≈ 2) containing a small Prandtl number fluid ($\sigma < 0.026$) typical of molten metals and molten semiconductors. We use the Navier-Stokes and energy equations in the Boussinesq approximation to calculate numerically the basic steady states, analyze their linear stability, and compute some nonlinear secondary flows originated from the instabilities. All the calculated flows and the stability analysis are characterized by their symmetry properties. Due to the confined cylindrical geometry, -presence of lateral walls and lids-, all the flows are completely three dimensional even for the basic steady states. In the range of Prandtl numbers studied, we have identified four different types of instabilities, either oscillatory or stationary. The physical mechanisms, shear or buoyancy, of the corresponding flow transitions have been analyzed. As the value of the Prandtl number approaches $\sigma = 0.026$ the scenario of bifurcations becomes more complicated due to the existence of two different stable basic states originated in a saddle-node bifurcation; a fact that had been overlooked in previous works. [http://dx.doi.org/10.1063/1.4856615]

I. INTRODUCTION

The problem of convection induced by a lateral temperature gradient has been extensively studied during the last decades. The main interest in studying this system comes from heat transfer problems of industrial interest and from the study of the melt zone in crystal growth processes such as the horizontal Bridgman method. In this latter problem, crystals grown from the melt can present inhomogeneities in the form of striations, caused by oscillatory variations of the concentration in the solidification front.[1] For this reason many studies have focused on the study of the oscillatory threshold in low Prandtl number fluids in different geometrical configurations.[2] The system is also interesting from a fundamental fluid dynamics point of view, since it exhibits a rich nonlinear behavior that leads to complex spatiotemporal dynamics.[3]

Some simplified geometries have been considered in the theoretical study of natural convection induced by a horizontal temperature gradient. In one of such simplifications a channel is considered; the container is supposed to be unbounded in one horizontal direction, and a constant horizontal temperature gradient is applied to the lateral boundaries. The basic state in this configuration is a parallel flow known as Hadley circulation,[4] in which the fluid moves in the direction of the temperature gradient in the lower part of the channel, and in the opposite direction in the upper part, leading to a stable temperature stratification. This problem has been studied both in two dimensions,[5] and in three dimensional rectangular[6] and cylindrical[7] geometries. In this problem, the stability of the basic flow is considered against perturbations periodic in the streamwise direction. Some of the results have been reviewed in the context of crystal growth technologies in Ref. 8.

[a] maria.isabel.mercader@upc.edu
[b] odalys.sanchez@upc.edu
[c] oriol@fa.upc.edu

Other authors have considered bounded geometries; in these cases the temperature gradient is imposed by setting a temperature difference between the two opposing lateral walls. The problem of a bounded domain has been intensely investigated in two dimensions,[9,10] and has even been used as a benchmark for testing two dimensional Boussinesq codes.[11,12] The works considering three dimensional cavities are less abundant. Some works dealt with bounded 3D boxes filled with air[13] or a low Prandtl number fluid.[14,15] Some experimental results using gallium as a low Prandtl number fluid have been compared to numerical simulations.[16,17] All the emphasis has been put in identifying secondary bifurcations, specially the ones leading to oscillatory secondary flows. Although bounded cylindrical geometries represent more realistically the melt zone in the horizontal Bridgman crystal growth process, this configuration has barely been studied. In this paper we will consider cylinders of moderate aspect ratio, as the ones studied before in Ref. 18, and we will focus on the Prandtl number dependence of the first instability of the basic state in the range $\sigma < 0.026$, the value used in Ref. 18, corresponding to molten metals and semiconductors.

The paper is organized as follows. In Sec. II the problem is stated; we present the model equations in Sec. II A, the numerical methods used in Sec. II B, and in Sec. II C we describe the symmetries of the problem and characterize the basic flow. In Sec. III we show and discuss the results of the work; in Sec. III A we analyze the case $\sigma = 0.00715$ by varying the aspect ratio of the cylinder ($\Gamma =$ height/diameter) around $\Gamma = 2$, in Sec. III B the linear stability analysis is performed for the full range of Prandtl numbers considered, and Sec. III D is devoted to the computation and description of the saturated secondary flows for four selected Prandtl numbers representative of the different instabilities found in Secs. III B–III C. Finally, we outline the relevance of our results in Sec. IV.

II. THE PHYSICAL PROBLEM

A. Equations and boundary conditions

We consider Boussinesq convection in a horizontal cylinder of length H and radius R in the presence of a vertical gravitational force. The axis of the cylinder is on the z-axis, the origin of coordinates is taken on the left lid and the gravitational force in the x-direction, $\mathbf{g} = g\hat{\mathbf{x}}$. The cylinder is heated from the left, ΔT being the temperature difference between the lids of the cylinder (see Fig. 1). We split the temperature field in two parts, a linear profile and a fluctuation

$$T = T_c + \Delta T(1 - z/H + \Theta),$$

where T_c is the temperature at the cold lid ($z = H$).

Scaling lengths with a reference length l, time with the thermal diffusion time l^2/κ, κ being the thermal diffusivity, and temperature with ΔT, the nondimensional equations that describe the evolution of the velocity field $\mathbf{u}$ and the deviation of the temperature Θ from the linear profile, are

$$\nabla \cdot \mathbf{u} = 0, \tag{1a}$$

$$\partial_t \mathbf{u} + (\mathbf{u} \cdot \nabla)\mathbf{u} = -\nabla p + \sigma \nabla^2 \mathbf{u} + Ra\sigma\left(\frac{l}{H}z - \Theta\right)\hat{\mathbf{x}}, \tag{1b}$$

$$\partial_t \Theta + (\mathbf{u} \cdot \nabla)\Theta = w\frac{l}{H} + \nabla^2 \Theta, \tag{1c}$$

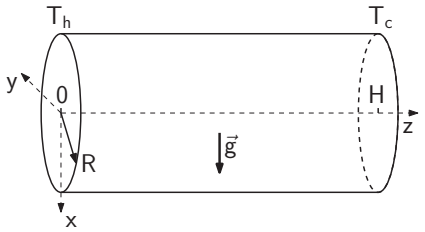

FIG. 1. Configuration of the horizontal cylinder laterally heated and reference frame. Notice that the gravity field is parallel to x-axis.

where w is the z-component of the velocity field. The two dimensionless numbers that describe thermal convection are the Rayleigh number Ra, and the Prandtl number σ, defined as

$$Ra = \frac{\alpha \Delta T g l^3}{\kappa \nu}, \quad \sigma = \frac{\nu}{\kappa}, \tag{2}$$

where α is the thermal expansion coefficient and ν is the kinematic viscosity. The Rayleigh number is the control parameter of the system and measures the strength of the imposed temperature gradient, and the Prandtl number relates momentum diffusion to thermal diffusion.

We consider no-slip and fixed temperature boundary conditions at the left and right lids of the horizontal cylinder and no-slip and insulating boundary conditions on the lateral wall,

$$\mathbf{u} = \Theta = 0 \qquad \text{on} \qquad z = 0, H/l, \tag{3a}$$

$$\mathbf{u} = \partial_r \Theta = 0 \qquad \text{on} \qquad r = R/l. \tag{3b}$$

As a measure of the strength of convection we will use the dimensionless mean kinetic energy defined as

$$E_k = \frac{\int_0^{2\pi} \int_0^{R/l} \int_0^{H/l} \mathbf{u} \cdot \mathbf{u} \; r \, \mathrm{d}r \, \mathrm{d}\theta \, \mathrm{d}z}{2\pi (R/l)^2 (H/l)}. \tag{4}$$

To ease the comparison with the 2D case, we have chosen as reference length the diameter of the cylinder $l = 2R$ and have defined the aspect ratio Γ of the cylinder as $\Gamma = H/(2R)$.

The previous non-dimensional equations for the velocity field $\mathbf{u} = (u, v, w)$ in cylindrical coordinates (r, θ, z) are written as follows:

$$\nabla \cdot \mathbf{u} = 0, \tag{5a}$$

$$\partial_t u + [(\mathbf{u} \cdot \nabla)\mathbf{u}]_r = -\partial_r p + \sigma [\nabla^2 \mathbf{u}]_r + Ra\sigma (z/\Gamma - \Theta) \cos\theta, \tag{5b}$$

$$\partial_t v + [(\mathbf{u} \cdot \nabla)\mathbf{u}]_\theta = -\frac{1}{r} \partial_\theta p + \sigma [\nabla^2 \mathbf{u}]_\theta - Ra\sigma (z/\Gamma - \Theta) \sin\theta, \tag{5c}$$

$$\partial_t w + [(\mathbf{u} \cdot \nabla)\mathbf{u}]_z = -\partial_z p + \sigma [\nabla^2 \mathbf{u}]_z, \tag{5d}$$

$$\partial_t \Theta + (\mathbf{u} \cdot \nabla)\Theta = w/\Gamma + \nabla^2 \Theta. \tag{5e}$$

B. Numerical methods

The system of equations (5) and boundary conditions (3) has been solved numerically using the algorithm described in Ref. 19, which can be summarized as follows. To integrate the equations in time, we use the second order time-splitting method proposed in Ref. 20 combined with a pseudo-spectral method for the spatial discretization, Galerkin-Fourier in the azimuthal coordinate θ and Chebyshev collocation in r and z. The radial dependence of the functions is approximated by a Chebyshev expansion between $-R$ and R, but forcing the proper azimuthal parity of the variables at the origin.[21,22] For instance, the scalar field Θ and the axial velocity w have an even parity ($\Theta(-r, \theta) = \Theta(r, \theta + \pi)$), whereas u and v are odd functions. To avoid including the origin in the mesh grid, we use an odd number of Gauss-Lobatto points in r, and we enforce the equations only in the interval $(0, R]$. We use the standard combination $u_+ = u + iv$ and $u_- = u - iv$ in order to obtain, as a result of the splitting, Helmholtz equations for all the variables Θ, w, u_+ and u_-. For each Fourier mode, these equations are solved using a diagonalization technique in the two coordinates r and z. The imposed parity of the functions guarantees the regularity conditions at the origin needed to solve the Helmholtz equations.[23] The same numerical code has been used by the

authors and collaborators to study other problems in convection in vertical cylinders, such as binary fluid convection[24] and rotating convection.[25,26]

Steady solutions have been computed with Newton's method. We have used a first-order version of the time-stepping code described above for the calculation of a Stokes preconditioner that allows a matrix-free inversion of the preconditioned Jacobian needed in each Newton iteration.[27] The corresponding linear system is solved by an iterative technique using a GMRES package.[28] The left-hand side of the preconditioned linear system (Jacobian acting on the correction) corresponds to one time step of the linearized equations and the right-hand side corresponds to performing one time step of the full nonlinear equations. In this way the Jacobian matrix is never constructed or stored.[27]

Regarding the linear stability analysis of the steady states, once they have been calculated by the method described before, estimations of eigenvalues and eigenvectors of the linearized problem have been obtained by using Arnoldi's method. The method is applied to calculate the dominant eigenvalues of the exponential of the Jacobian, which can be trivially related to the leading eigenvalues, i.e., with the largest real part of the Jacobian. To this end, the algorithm for the time stepping of the linearized equations has been used, since, in fact, it approximates the action of the exponential transformation of the Jacobian on the solution at the previous time step. The eigensolving itself has been implemented using the ARPACK package. To determine eigenvalues and eigenvectors accurately, we use the estimated eigenvalues and eigenvectors as the initial guess to solve, via a Newton's method, the nonlinear system (eigenvalues are also unknowns) derived from the eigenvalue problem. Once the dominant eigenvalue is identified, a secant method is used to obtain the critical Rayleigh numbers (real part of the eigenvalue equal to zero) and frequencies at the bifurcation points.

An alternative method to carry out the linear stability analysis uses the property that bifurcations are typically associated with the breaking of symmetries of the state that is destabilized. We built some variables associated to the symmetries of the state, which are zero if a symmetry is present, and we monitor their value. When the instability triggers on, we can easily detect the growth of these variables, however small they are. The linear growth and frequencies of these small variables can be calculated for fixed control parameters. Using different points, we use a secant method to obtain the bifurcation point.

In the results reported in the present paper we have used a resolution that ensures variations of the values of Rayleigh number and frequency at the bifurcation points smaller than 0.1%. We have used a grid of $n_r = 32$, $n_z = 52$, $n_\theta = 52$ points in the radial, axial, and azimuthal directions respectively for small values of the Rayleigh number (smaller than 7×10^3) and $n_r = 48$, $n_z = 64$, $n_\theta = 64$ for higher values. In time integration we have used a time step $\Delta t = 5 \times 10^{-5}$.

C. Symmetries and the basic state

Equations and boundary conditions are equivariant under the group of symmetries G that contains the transformations $\{I, R_1, R_2, R_3\}$, where I stands for the identity, R_1 is a reflection with respect to the middle longitudinal vertical plane ($y = 0$), which will be denoted by L_v plane, R_2 is a point symmetry with respect to the center of the cylinder and R_3, which is the composition of the previous transformations, is a rotation by π about the line $x = 0$, $z = \Gamma/2$, the diameter parallel to the y-axis located in the center of the cylinder. The G-group has three subgroups $\{I, R_1\}$, $\{I, R_2\}$, and $\{I, R_3\}$, which are all different but isomorphic to $\mathbf{Z}_2$. In addition G can be generated by combining any two of these three $\mathbf{Z}_2$ subgroups, so we write $G = \mathbf{Z}_2 \otimes \mathbf{Z}_2 \equiv D_2$ where $\otimes$ indicates the direct product of the groups, used when each element of either group commutes with every element of the other group. These transformations act on the cylindrical components of the velocity field and deviation of the temperature u, v, w, Θ as follows:

$$R_1 : (r, \theta, z) \to (r, -\theta, z), \qquad (u, v, w, \Theta) \to (u, -v, w, \Theta), \tag{6}$$

$$R_2 : (r, \theta, z) \to (r, \theta + \pi, \Gamma - z), \qquad (u, v, w, \Theta) \to (u, v, -w, -\Theta), \tag{7}$$

$$R_3 : (r, \theta, z) \to (r, \pi - \theta, \Gamma - z), \qquad (u, v, w, \Theta) \to (u, -v, -w, -\Theta). \tag{8}$$

When expressed in rectangular coordinates these transformations act as follows:

$$R_1 : (x, y, z) \to (x, -y, z), \qquad (v_x, v_y, v_z, \Theta) \to (v_x, -v_y, v_z, \Theta), \tag{9}$$

$$R_2 : (x, y, z) \to (-x, -y, \Gamma - z), \qquad (v_x, v_y, v_z, \Theta) \to (-v_x, -v_y, -v_z, -\Theta), \tag{10}$$

$$R_3 : (x, y, z) \to (-x, y, \Gamma - z), \qquad (v_x, v_y, v_z, \Theta) \to (-v_x, v_y, -v_z, -\Theta). \tag{11}$$

Equivariance of equations and boundary conditions under a given transformation, i.e., R_1, means that if the field $\Psi = (u(r, \theta, z), v(r, \theta, z), w(r, \theta, z), \Theta(r, \theta, z))$ is a solution, then the field $R_1\Psi = (u(r, -\theta, z), -v(r, -\theta, z), w(r, -\theta, z), \Theta(r, -\theta, z))$ is also a solution of the problem. These two solutions are not required to be the same. If so, we say that the solution possesses R_1 symmetry, because it is invariant under the transformation R_1.

This system is equivariant under the same group of symmetries as the two dimensional Rayleigh-Bénard convection in a rectangular enclosure with up-down and left-right symmetric boundary conditions. Thus, the classification of the bifurcations of the primary solutions studied extensively in the 2D domain can be directly applied to the cylinder. However, it is important to remark that, contrary to what happens in Rayleigh-Bénard convection, the quiescent state is not a solution of equations and boundary conditions; therefore, fluid motion is present without the need to overcome a threshold value of any parameter. The steady state, obtained for small values of the Rayleigh number, is invariant with respect to all the symmetries of the problem and will be called the *basic state*.

In Figs. 2 and 3 we show the basic state obtained for $\Gamma = 2$, Prandtl number $\sigma = 0.00715$ and Rayleigh number $Ra = 1885$. In order to make the symmetries of this solution explicit, we represent in Fig. 2 (top) the transverse flow $u\hat{\rho} + v\hat{\theta}$, where $\hat{\rho}$ and $\hat{\theta}$ are the radial and azimuthal unit vectors, in three vertical planes $z = 0.05\Gamma, \Gamma/2, 0.95\Gamma$. For the sake of clarity, we have not used the same scale for the length of the arrows in each figure. For this solution, the maximum transverse velocity in the cross-sections at $z = 0.05\Gamma$ and $z = 0.95\Gamma$ is approximately five times larger than in the $z = \Gamma/2$ plane. It should be noticed that the azimuthal component v of the velocity in the longitudinal plane L_v, is zero due to the R_1 symmetry. In Figs. 2 (bottom) and 3 we show the contour plots of the axial velocity w and the temperature deviation Θ at the same transverse cross sections in the cylinder. Dark (light) shadow is related with positive (negative) values. The symmetries also force the azimuthal and axial components of the velocity (v, w) and the temperature deviation Θ to be always zero in the horizontal diameter of the $z = \Gamma/2$ cross section vertical plane. In agreement with its boundary condition, the temperature deviation Θ is very small near the lids. A more detailed description of this flow will be given in Sec. III A.

III. RESULTS

We present here results devoted to analyze the primary bifurcation of the basic flow for small values of Prandtl number and a cylinder of aspect ratio around 2. We aim to characterize the basic flow at the bifurcation point, the type of bifurcation and the secondary flows near the critical points. The values of the Prandtl number considered in this work are smaller than $\sigma = 0.026$, the value used in the work of Vaux *et al.*[18] We start the section with a study of the stability of the basic state for a fluid with $\sigma = 0.00715$ and aspect ratio in the range $1.5 < \Gamma < 2.5$ to make a comparison with our previous results on a rectangular box of the same aspect ratio.[10] Second, we present the results that show the effect of the Prandtl number in the stability of the basic flow for a fixed value of the aspect ratio $\Gamma = 2$. We finish the section by analyzing secondary flows near the critical points, which are associated with the breaking of different symmetries of the basic flow when the Prandtl number varies.

A. Basic flow and its linear stability for $\sigma = 0.00715$, $\Gamma = [1.5 - 2.5]$

We describe the structure of the basic flow and the stability properties for $\sigma = 0.00715$ (representative of a molten metal or semiconductor at high temperature), and $\Gamma \in [1.5, 2.5]$. First, we

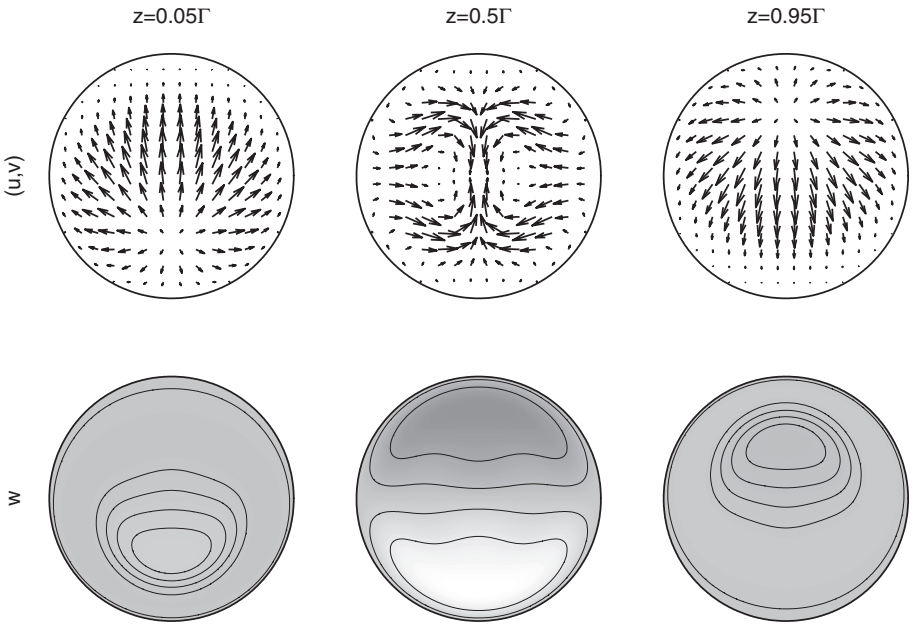

FIG. 2. Transverse flow (top) and contour plots of the axial velocity w (bottom) in the cross section vertical planes $z = 0.05\Gamma$, $z = \Gamma/2$, and $z = 0.95\Gamma$. The positive z-axis, perpendicular to the paper, points downwards ($\sigma = 0.00715$, $Ra = 1885$, $\Gamma = 2$).

discuss in more detail for the parameters $Ra = 1885$, $\Gamma = 2$ the structure of the basic flow which has already been introduced in Sec. II C. Transverse sections of the basic flow are shown in Fig. 2. For this solution the maximum axial velocity in nondimensional units is $w = 2.7$ and is located at cross section $z = 0.56\Gamma$, in the vertical diameter near $r = 0.71R$. The maximum transverse velocity value $v_t = 1.8$ is located at cross section $z = 0.97\Gamma$, in the vertical diameter, now closer to the center, at $r = 0.17R$. In cross section $z = \Gamma/2$, four vortices near the horizontal diameter appear. In this line the fluid circulates radially from the walls towards the stagnation points, which are located near the center of the cross section ($r \approx 0.26R$). The maximum radial velocity in this horizontal line is $u \approx -0.17$ and occurs at $r \approx 0.71R$. In the vertical diameter, the fluid circulates from the wall to the center, in contrast to what happens in the perfectly conducting cylindrical channel subjected to a longitudinal temperature gradient.[7]

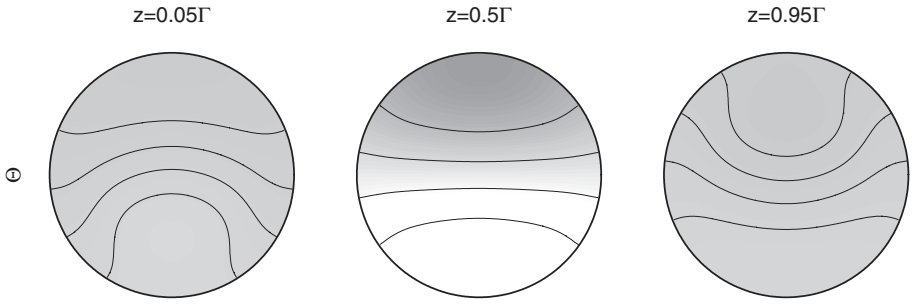

FIG. 3. Contour plots of the deviation of the temperature in the cross section vertical planes $z = 0.05\Gamma$, $z = \Gamma/2$, and $z = 0.95\Gamma$ ($\sigma = 0.00715$, $Ra = 1885$, $\Gamma = 2$).

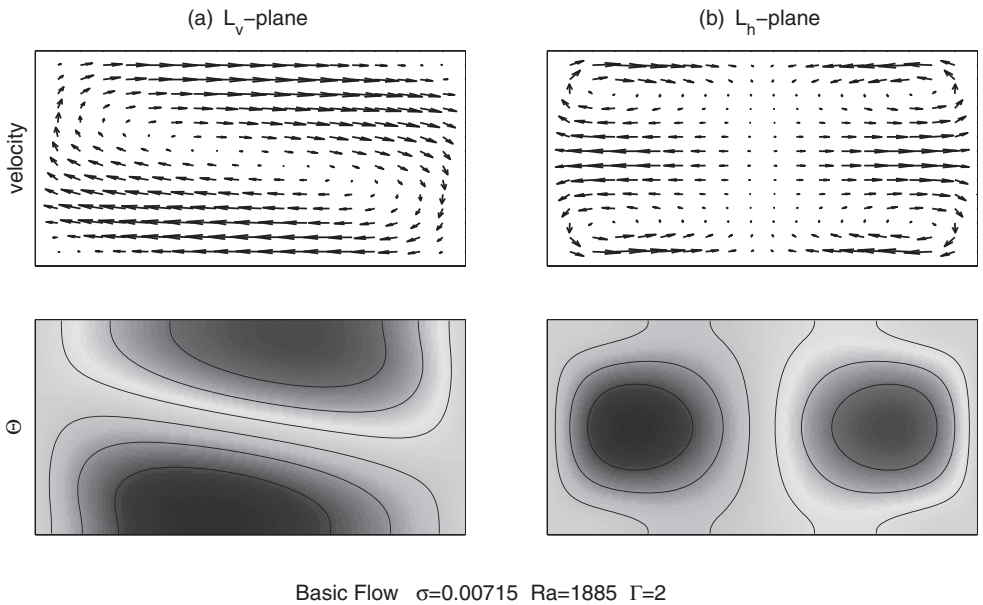

FIG. 4. (a) Velocity field (top) and contour plot of the deviation of the temperature (bottom) in the longitudinal plane L_v, with the positive y-axis, perpendicular to the paper, pointing downwards; (b) projection of the velocity field and contour plot of the deviation of the temperature on the horizontal plane L_h, with the positive x-axis, perpendicular to the paper, pointing downwards ($\sigma = 0.00715$, $Ra = 1885$, $\Gamma = 2$).

In Fig. 4 (top, left), we show the vertical plane L_v; the velocity vectors display the well known large scale circulation, i.e., one loop with the fluid ascending along the hot wall, descending along the cold wall and moving longitudinally, creating a vertically stable stratification (see Fig. 3). As we have mentioned before, the R_1 symmetry forces the azimuthal component v of the velocity in this plane to be zero. We also show in Fig. 4 (top, right) the projection of the velocity field onto the horizontal plane $x = 0$ (L_h-plane), where four vortices are clearly identified. Notice that the axial velocity w of the flow near the axis of the cylinder is positive for $z > \Gamma/2$ and negative for $z < \Gamma/2$. This projection looks different from the velocity field for $\sigma = 0.026$ shown in Ref. 18, where in each half part of the cylinder the axial velocity changes sign. We will discuss further the connection between these two solutions. The maximum value of the velocity in the longitudinal plane L_v is $v_l = 2.7$ and the maximum value of the projection of the velocity onto the horizontal plane L_h is $v_h = 1.15$ (we use different scales associated to the length of the arrows in both figures).

In Fig. 4 (bottom, left), we display the contour plot of the deviation of temperature Θ in the vertical plane L_v, which shows that the temperature of the flow is hotter than the linear profile in the upper part and colder in the lower part, creating the vertically stable stratification. The deviation of temperature in this plane varies between ± 0.074. In Fig. 4 (bottom, right) we show, with a different scale of gray-levels, the contour plot of Θ in the horizontal plane, which varies between ± 0.018. Notice that when using projections of the velocity field on the rectangular L_v and L_h planes or contour plots of the deviation of temperature in these planes, in the L_v plane both symmetries R_2 and R_3 act as reflection symmetries with respect to the center of the rectangle. In the L_h plane, the R_3 (R_1) symmetry acts as a reflection with respect to a vertical (horizontal) line through the center of the rectangle and the R_2 symmetry as a reflection with respect to the center of the rectangle.

The stability of the above basic flow is analyzed for a fixed value of the Prandtl number $\sigma = 0.00715$ and a range of aspect ratios between $\Gamma = 1.5$ and $\Gamma = 2.5$. We aim to compare with previous results obtained in a rectangular domain[10] and a Prandtl number of the same order of magnitude. In the rectangular case, the basic solution is R_c-invariant, with R_c being a reflection symmetry with respect to the center of the rectangle and it loses stability in a supercritical Hopf bifurcation that maintains the reflection symmetry R_c. In the cylinder, the primary instability is oscillatory, supercritical and maintains only the R_3 symmetry. In the rectangular longitudinal plane

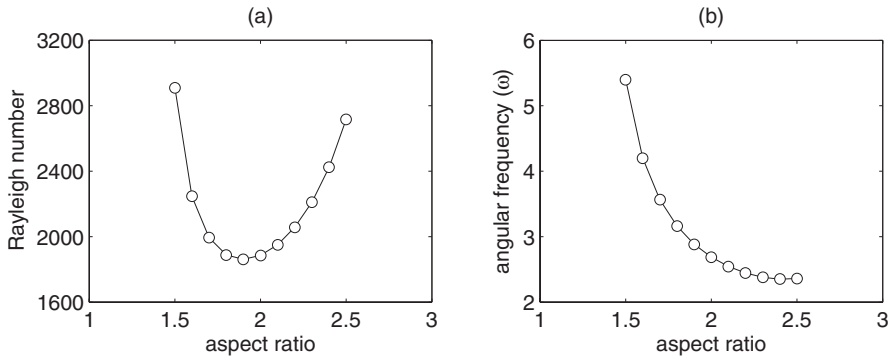

FIG. 5. (a) Critical Rayleigh number and (b) frequency for the primary bifurcation of the basic flow as a function of the aspect ratio for Prandtl number $\sigma = 0.00715$.

L_v of the cylinder, the R_3 transformation acts over the rectangular components of the velocity field in this plane v_x, v_z and over the deviation of temperature Θ, in the same way as the R_c transformation in the rectangular domain does.[10] However, due to the fact that R_1 symmetry is not maintained, the eigenvector is antisymmetric with respect to this symmetry,[29] forcing the eigenvector components of the velocity field in this plane v_x, v_z and deviation of the temperature Θ, to be zero. So, for these parameters, the primary instability in the cylinder is different than in the rectangular case. In fact, to recover the rectangular R_c symmetry, it would be necessary that the R_1 symmetry was also maintained. Only instabilities that maintain all the symmetries of the group are equivalent to the R_c-symmetric instability of the rectangular case.

The critical Rayleigh numbers and the corresponding Hopf frequencies are shown in Fig. 5. Despite the different type of symmetry, we observe a dependence on the aspect ratio similar to the rectangular case. The values of the critical Rayleigh number and Hopf frequencies are also of the same order; for instance, in a rectangular cavity of aspect ratio $\Gamma = 2$ the critical Rayleigh number and Hopf frequency we obtained were $Ra_c = 2.381 \times 10^3$ and $\omega_c = 6.04$, comparable with the values in the cylinder $Ra = 1.885 \times 10^3$ and $\omega_c = 2.69$.

In the rectangular case, beyond the supercritical primary bifurcation, stable reflection symmetric periodic solutions exist until a Neimark-Sacker bifurcation occurs at $Ra_2 \approx 2.62 \times 10^4$ and the secondary quasiperiodic solutions are also reflection symmetry invariant.[10] In the cylinder a secondary bifurcation occurs at a value of the Rayleigh number significantly lower than in the rectangular case, $Ra_2 \approx 3100$, and this secondary instability is a supercritical pitchfork bifurcation that breaks the remaining R_3 symmetry and which gives rise to a synchronous non-symmetric periodic solution.

B. Linear stability analysis of the basic flow: $\Gamma = 2$ and $\sigma = [0 - 0.0249]$

As it is well known in this problem, the instabilities of the symmetric basic steady state can either be steady or oscillatory, preserving one of the symmetries and breaking the other two (with antisymmetric eigenvectors with respect to the broken symmetries); or they can be oscillatory maintaining all the symmetries.[15] Obviously, a saddle node bifurcation (a steady bifurcation maintaining all the symmetries) is also possible. In this section we present the results corresponding to the linear stability analysis of the basic flow contained in a cylinder of aspect ratio $\Gamma = 2$ and Prandtl numbers smaller than 0.0249. The results corresponding to the linear stability analysis of the basic flow in the range of values from $\sigma = 0.0249$ to the value used in the work of Ref. 18, $\sigma = 0.026$, will be discussed in Sec. III C. Fig. 6(a), which summarizes the dependence of the critical Rayleigh number on the value of the Prandtl number, reveals that three different types of instabilities become dominant in this region. Two of them are oscillatory, one preserving only the R_3 symmetry of the basic state and the other maintaining all the symmetries, G. The third type of instability is steady and preserves only the R_1 symmetry. The corresponding frequencies are plotted in Fig. 6(b). The frequencies of the

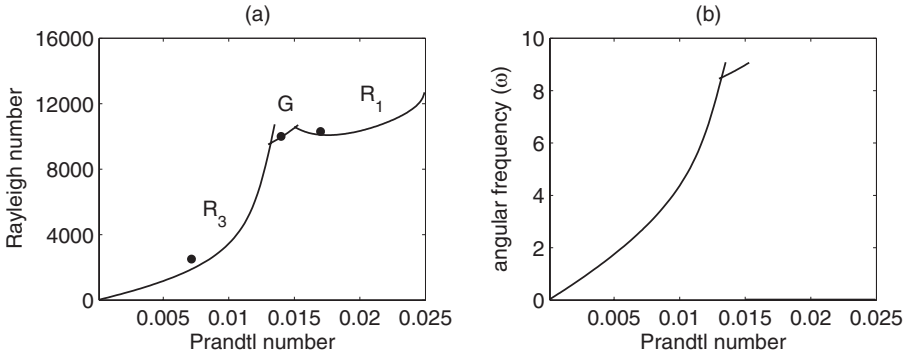

FIG. 6. (a) Critical Rayleigh number and (b) frequency for the primary bifurcation of the basic state. R_3 (R_1) stands for bifurcations that only respect the reflection symmetry R_3 (R_1) of the basic state; G if all symmetries of the basic flow are maintained ($\Gamma = 2$). The filled circles in (a) indicate the points where secondary flows have been calculated in Sec. III D.

dominant eigenmodes of each type of oscillatory instabilities are continuous functions of the Prandtl number, which means that the dominant oscillatory eigenmode of each type, R_3 or G, is always the same. From $\sigma = 0.0149$ the frequency is null since the instability that preserves the R_1 symmetry is steady. We want also to remark that at the double Hopf point located near $\sigma = 0.0132$, where the two oscillatory instabilities that maintain R_3 symmetry only and all the symmetries G bifurcate, the frequencies of the two unstable modes have almost the same value; then the double Hopf point is close to being resonant.

For $\sigma \leq 0.0132$ the instability is oscillatory, it preserves the R_3 symmetry of the basic flow and breaks the R_1 and R_2 symmetries. In Fig. 7 (left), we display the contour plots of the real and imaginary parts of the deviation of temperature of the dominant eigenvector for $Ra = 1885$ and $\sigma = 0.00715$ in two vertical cross sections at distances $z = \Gamma/4$ and $3\Gamma/4$ from the hot lid. In these plots the positive x-axis is directed to the bottom, and the positive z-axis, which is perpendicular to the paper, points downwards. This choice will be maintained in all the figures in which vertical cross sections of eigenvectors are plotted. The temperature deviation satisfies

$$\Theta(r, \theta, z) = -\Theta(r, -\theta, z), \qquad \text{i.e.,} \qquad R_1\Theta = -\Theta, \tag{12}$$

$$\Theta(r, \theta, \Gamma/4) = +\Theta(r, \theta + \pi, 3\Gamma/4), \qquad \text{i.e.,} \qquad R_2\Theta = -\Theta, \tag{13}$$

$$\Theta(r, \theta, \Gamma/4) = -\Theta(r, \pi - \theta, 3\Gamma/4), \qquad \text{i.e.,} \qquad R_3\Theta = +\Theta. \tag{14}$$

In Fig. 7(right), where the same field is displayed in the horizontal plane L_h ($x = 0$), the antisymmetric nature of the field with respect to R_1 and R_2 transformations can be observed. Notice that the scale associated to gray-levels in Fig. 7 is different for the cross sections and the horizontal plane. For this critical mode, as a consequence of the breaking of R_1 symmetry, the deviation of temperature is null in the vertical plane L_v ($y = 0$).

For values of the Prandtl number lower than $\sigma = 10^{-4}$, we have used the viscous time to obtain the dimensionless equations.[15] For these values the instability we have described continues to be dominant. The critical values of the Rayleigh number and the Hopf frequencies satisfy $Ra_c/\sigma \approx 1.974 \times 10^5$ and $\omega_c/\sigma \approx 314.4$ in agreement with the values that we have obtained for the limit case $\sigma = 0$. This result differs from that obtained in a square cross section channel subjected to a horizontal temperature gradient.[6] The authors obtain that the dominant instability is steady and maintains the symmetry with respect to the vertical plane, which is equivalent to our R_1 symmetry. Our results for very small Prandtl number also differ from the work of Henry and BenHadid[15] in 3D rectangular cavities. In this paper, for a cavity with rectangular cross-section 2×1 and length 4, an oscillatory instability that maintains a symmetry equivalent to R_2 is obtained. These discrepancies are not surprising, an agreement between our results and those of referred works was not really

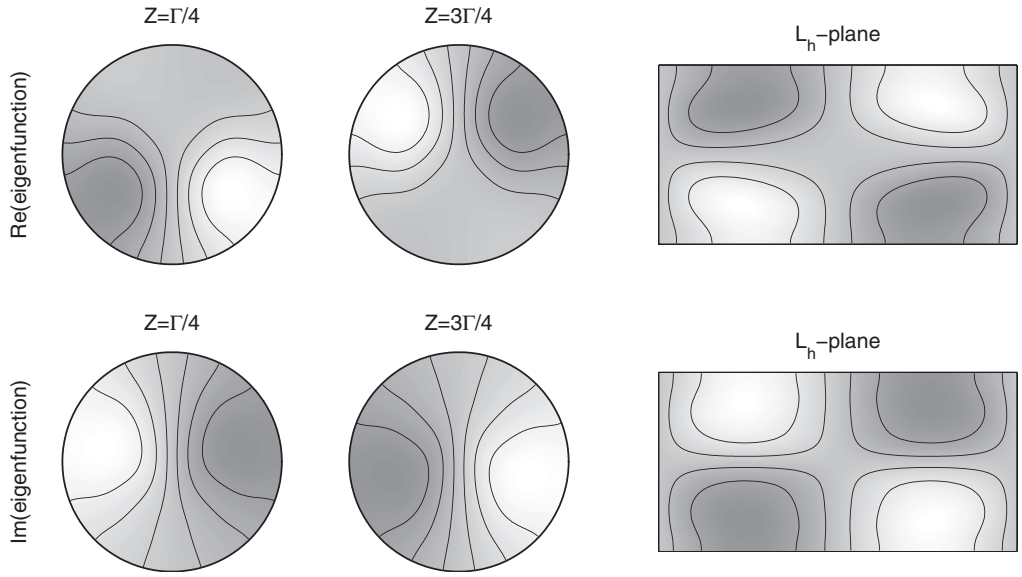

FIG. 7. Eigenvector responsible for the instability at the critical point $\sigma = 0.00715$, $Ra = 1885$. The instability is oscillatory, preserves the R_3 symmetry of the basic flow and breaks the R_1 and R_2 symmetries. Real and imaginary part of the temperature deviation: (left) in two cross sections at distances $z = \Gamma/4$, $3\Gamma/4$ of the hot lid (the positive x-axis is directed to the bottom, and the positive z-axis, perpendicular to the paper, points downwards), (right) in the horizontal plane L_h (the positive x-axis, perpendicular to the paper points downwards). Gray-levels for cross sections and horizontal planes plots have different scales. $\Gamma = 2$.

expected because the geometry is very different. This fact reveals that it plays an important role in this problem.

From $\sigma = 0.0132$ to $\sigma = 0.0149$ the instability is oscillatory and preserves all the symmetries of the basic flow. As representative of this type of instability we display in Fig. 8(left) the real and imaginary parts of the deviation of temperature of the dominant eigenvector in two cross sections at distances $z = \Gamma/4$, $3\Gamma/4$ of the hot lid. The critical point values are $Ra = 9.967 \times 10^3$ and $\sigma = 0.014$ and the Hopf frequency is $\omega = 8.70$. The temperature deviation satisfies now

$$\Theta(r, \theta, z) = \Theta(r, -\theta, z), \qquad \text{i.e.,} \qquad R_1\Theta = +\Theta, \tag{15}$$

$$\Theta(r, \theta, \Gamma/4) = -\Theta(r, \theta + \pi, 3\Gamma/4), \qquad \text{i.e.,} \qquad R_2\Theta = +\Theta, \tag{16}$$

$$\Theta(r, \theta, \Gamma/4) = -\Theta(r, \pi - \theta, 3\Gamma/4), \qquad \text{i.e.,} \qquad R_3\Theta = +\Theta. \tag{17}$$

We also show in Fig. 8(right) the eigenvector temperature deviation contour plots in the vertical plane L_v ($y = 0$), which it is not null now. It is important to mention that if we multiply the complex eigenvector by an appropriate phase and represent the deviation of the temperature and the projection of the velocity field on this L_v-plane, we obtain a structure which is quite similar to the dominant eigenmode obtained for $\sigma = 0.00715$ in the rectangular case.

From $\sigma = 0.0149$ to $\sigma = 0.0249$ the instability is stationary, it preserves the R_1 symmetry of the basic flow and breaks the R_2 and R_3 symmetries. The dominant critical mode in this region is always the same (transitions cannot be inferred from discontinuities in the frequency). To show the symmetry properties of the eigenvector, we display in Fig. 9(left) the contour plot of the real part of the deviation of the temperature of the critical mode for $Ra = 1.005 \times 10^4$ and $\sigma = 0.017$. It is easy

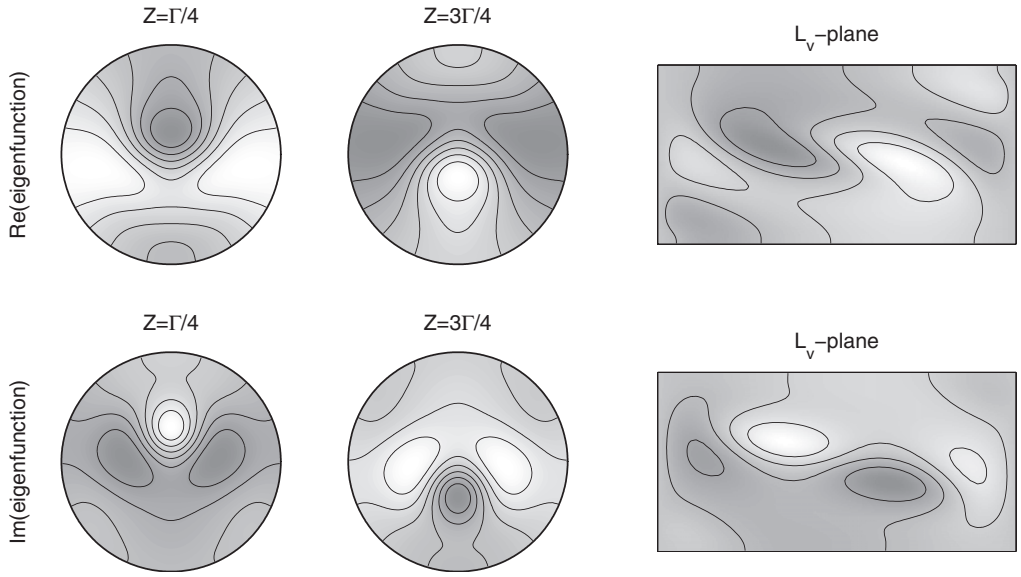

FIG. 8. Eigenvector responsible for the instability at the critical point $\sigma = 0.014$, $Ra = 9.967 \times 10^3$. The instability is oscillatory and preserves all the symmetries of the basic flow. Real and imaginary parts of the temperature deviation: (left) in two cross sections at distances $z = \Gamma/4$, $3\Gamma/4$ of the hot lid, (right) in the longitudinal plane L_v (the positive y-axis, perpendicular to the paper, points downwards). Gray-levels for cross sections and longitudinal plane plots have different scales. $\Gamma = 2$.

to notice that the temperature deviation satisfies

$$\Theta(r, \theta, z) = \Theta(r, -\theta, z), \qquad \text{i.e.,} \qquad R_1\Theta = +\Theta, \tag{18}$$

$$\Theta(r, \theta, \Gamma/4) = +\Theta(r, \theta + \pi, 3\Gamma/4), \qquad \text{i.e.,} \qquad R_2\Theta = -\Theta, \tag{19}$$

$$\Theta(r, \theta, \Gamma/4) = +\Theta(r, \pi - \theta, 3\Gamma/4), \qquad \text{i.e.,} \qquad R_3\Theta = -\Theta. \tag{20}$$

In Fig. 9(right) we show the deviation of temperature in the vertical plane L_v, where the antisymmetric character with respect to R_2 transformations can be appreciated. In the horizontal and vertical planes the contour plots for the deviation of temperature look very similar (not shown) due to the fact that this critical mode has a dominant axisymmetric contribution, as shown later. In Sec. III D we will see that the changes that this instability produces in the basic flow affect mainly the flow in the central part of the cylinder.

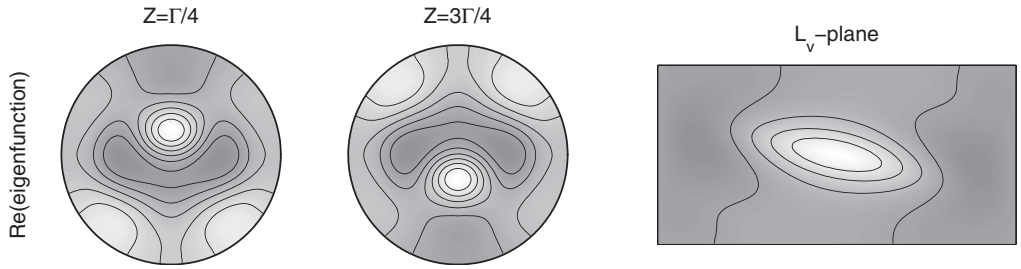

FIG. 9. Eigenvector responsible for the instability at the critical point $\sigma = 0.017$, $Ra = 1.005 \times 10^4$. The instability is steady, preserves the R_1 symmetry of the basic flow and breaks the R_2 and R_3 symmetries. Real part of the temperature deviation: (left) in two cross sections at distances $z = \Gamma/4$, $3\Gamma/4$ of the hot lid, (right) in the longitudinal plane L_v (the positive y-axis, perpendicular to the paper, points downwards). Gray-levels for cross sections and longitudinal plane plot have different scales. $\Gamma = 2$.

TABLE I. Preserved symmetry, Rayleigh number, Ra, Prandtl number, σ, normalized production of kinetic energy by shear associated with the eigenvectors at some bifurcation points, and main destabilizing term of the shear expansion in each case. $\Gamma = 2$.

Symmetry	Rayleigh number	Prandtl number	Normalized shear	Shear term
R_3	1.885×10^3	0.00715	1.027	$w'^* \frac{v'}{r} \frac{\partial W_0}{\partial \theta}$
R_3	3.450×10^3	0.01	1.041	$w'^* \frac{v'}{r} \frac{\partial W_0}{\partial \theta}$
R_3	8.888×10^3	0.013	1.045	$w'^* \frac{v'}{r} \frac{\partial W_0}{\partial \theta}$
G	9.967×10^3	0.014	1.029	$w'^* u' \frac{\partial W_0}{\partial r}$
R_1	1.005×10^4	0.017	1.031	$w'^* u' \frac{\partial W_0}{\partial r}$
R_1	1.267×10^4	0.02492	1.022	$w'^* \frac{v'}{r} \frac{\partial W_0}{\partial \theta}$
R_2	1.301×10^4	0.02492	1.024	$w'^* \frac{v'}{r} \frac{\partial W_0}{\partial \theta}$
R_2	1.396×10^4	0.026	1.023	$w'^* \frac{v'}{r} \frac{\partial W_0}{\partial \theta}$

1. Energy analysis

To analyze the physical mechanism of these three types of instabilities, we undergo a kinetic energy transfer analysis at some critical points.[30,18,15] We use the Reynolds-Orr equation obtained by integrating over the volume occupied by the fluid the inner product of the momentum equation for the perturbation and the perturbation of the velocity (critical eigenvector). If we denote by $[\mathbf{U_0}, T]$ the basic state and by $[\mathbf{u'}, \Theta']$ the eigenvector, the kinetic energy of the perturbation defined as $K = 1/2 \int_\Omega \mathbf{u'} \cdot \mathbf{u'}^* \, d\Omega$ satisfies

$$\frac{\partial K}{\partial t} = -\mathrm{Re}\left(\int_\Omega \mathbf{u}'^* \cdot (\mathbf{u}' \cdot \nabla \mathbf{U_0}) \, d\Omega\right) - \mathrm{Re}\left(\sigma \int_\Omega (\nabla \times \mathbf{u}') \cdot (\nabla \times \mathbf{u}'^*) \, d\Omega\right)$$
$$-\mathrm{Re}\left(Ra\, \sigma \int_\Omega \mathbf{u}'^* \cdot \Theta' \hat{\mathbf{x}} \, d\Omega\right).$$

The first term on the right-hand side represents the production of energy by shear, the second one is the viscous dissipation (which is always negative) and the third one is the production of energy by buoyancy. The terms with positive (negative) sign destabilize (stabilize) the basic flow. Since at the critical point the term on the left-hand side is zero, the shear term and the buoyancy term must balance the viscous dissipation. If we normalize the right-hand side terms with the absolute value of the viscous dissipation, the sum of shear and buoyancy terms must be 1.[15] In Table I we show the Rayleigh and Prandtl numbers at different critical points, the symmetry that is preserved and the value of the normalized shear term. The production of the kinetic energy of the perturbation in all these bifurcations clearly comes from the shear term (normalized shear larger than one). The buoyancy term is always negative (stabilizing), in agreement with the vertically stable stratification configurations of the basic flow. There are not important differences between the normalized values of the shear term in the range of Prandtl numbers analyzed, despite the different type of preserved symmetry and Rayleigh number values. However, the contributions of each term to the shear fluctuates. We have also indicated in Table I the main destabilizing parts of the shear term expansion in each case, although we have observed that, except in the instability that maintains the R_2 symmetry (described later), the mean value of the destabilizing terms $w'^* u' \frac{\partial W_0}{\partial r}$ and $w'^* \frac{v'}{r} \frac{\partial W_0}{\partial \theta}$ has the same order of magnitude. The maximum value of these destabilizing terms is always located near the center of the cylinder, away from the boundaries, indicating that the instability is originated in the bulk of the fluid and not in the boundary layers at the container walls. It is also worth mentioning the strong stabilizing contribution of the term $w'^* w' \frac{\partial W_0}{\partial z}$ at the critical points in which G and R_1 symmetries are preserved.

To gain some insight about the azimuthal structure of the eigenfunctions we have evaluated the contribution of the different azimuthal Fourier modes to the mean kinetic energy (4). From our Fourier expansion in the azimuthal coordinate, it is easy to split the mean kinetic energy by using

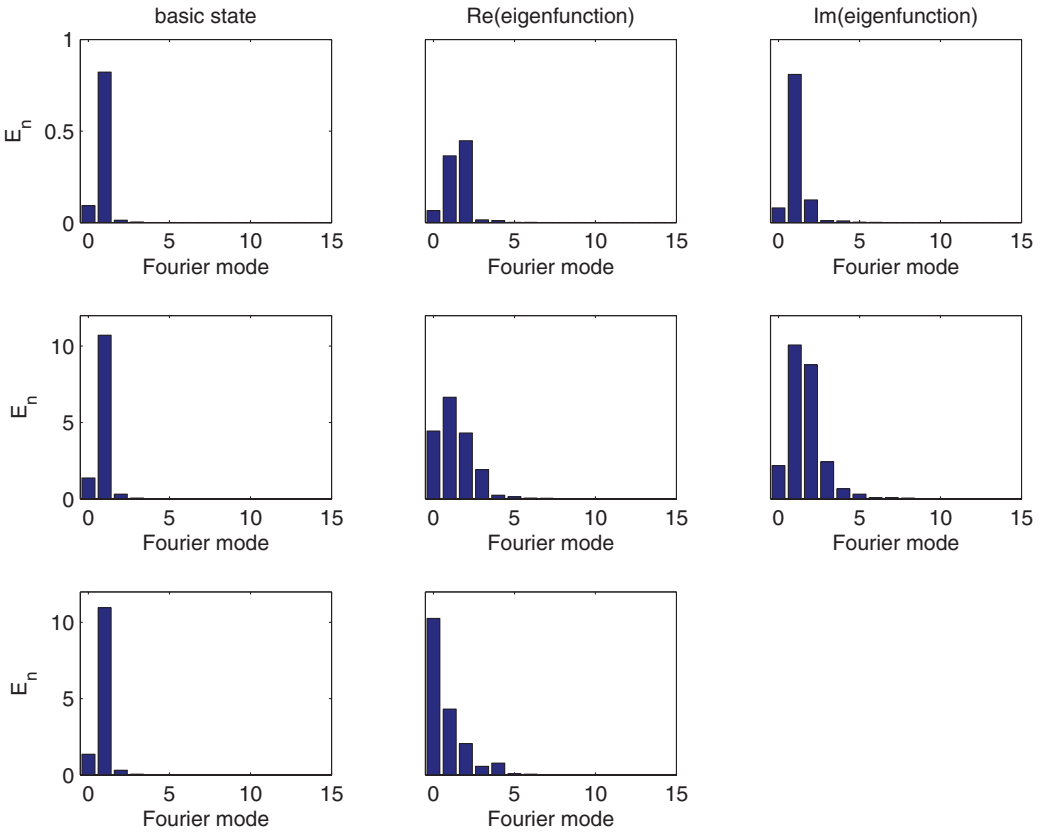

FIG. 10. Bar charts showing the azimuthal contribution E_n to the mean kinetic energy for the basic flow and for the real and imaginary parts of the critical mode at bifurcation points: from top to bottom ($Ra = 1885$, $\sigma = 0.00715$); ($Ra = 9.967 \times 10^3$, $\sigma = 0.014$); ($Ra = 1.005 \times 10^4$, $\sigma = 0.017$) real eigenvector.

the Parseval identity in this way

$$E_k = E_0 + \sum_{n=1}^{N} E_n$$

being

$$E_0 = \frac{\int_0^{R/l}\int_0^{H/l}(|\hat{u}_0|^2 + |\hat{v}_0|^2 + |\hat{w}_0|^2)\, r\, \mathrm{d}r\, \mathrm{d}z}{(R/l)^2(H/l)}, \quad E_n = \frac{2\int_0^{R/l}\int_0^{H/l}(|\hat{u}_n|^2 + |\hat{v}_n|^2 + |\hat{w}_n|^2\, r\, \mathrm{d}r\, \mathrm{d}z}{(R/l)^2(H/l)},$$

and where $|\hat{\phi}_n|$ refers to the n-complex Fourier coefficient of the function ϕ. We show some results of this analysis in Fig. 10, where we represent the bar charts for the basic flow and for the real and imaginary parts of the eigenvector in the bifurcation points representative of each type of instability that we have used previously. The scale of amplitude is only specified in the basic flow. The scale (not defined) for the real and imaginary part of every critical mode is the same.

We can infer from this analysis that the azimuthal structure of the basic flow is very similar in all three cases. It is dominated by a $n = 1$ mode and has a small contribution of the $n = 0$ mode, only the amplitude looks different. The critical mode that preserves R_3 symmetry ($Ra = 1885$, $\sigma = 0.00715$) is dominated by a $n = 1$ mode, but incorporates a significant contribution of mode $n = 2$. The critical mode that preserves all the symmetries ($Ra = 9.967 \times 10^3$, $\sigma = 0.014$) is dominated by modes $n = 1$ and $n = 2$ and incorporates significant contribution of modes $n = 0$ and $n = 3$. Finally, the real critical mode that preserves symmetry R_1 ($Ra = 1.005 \times 10^4$, $\sigma = 0.017$) is dominated by mode $n = 0$, with significant contributions of modes $n = 1, 2, 4, 3$ sorted by their intensity.

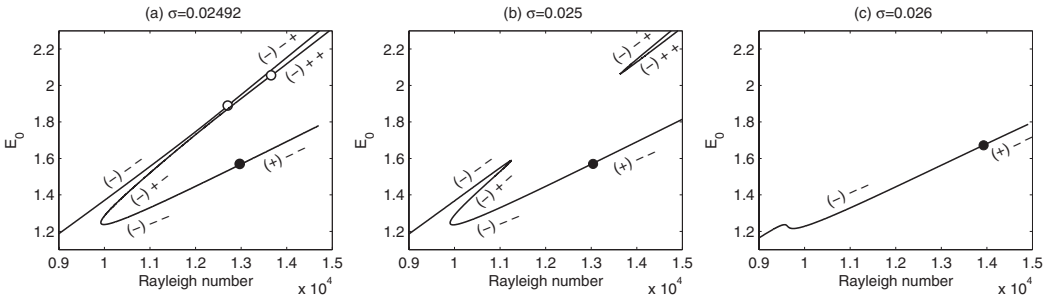

FIG. 11. Bifurcation diagrams showing the value of E_0 (contribution of zero-azimuthal modes to the mean value of the kinetic energy) of steady solutions that are G-symmetric as a function of the Rayleigh number for different values of the Prandtl number (a) $\sigma = 0.02492$, (b) $\sigma = 0.025$, (c) $\sigma = 0.026$. Open circles denote stationary bifurcations that preserve R_1 symmetry and the filled circle denotes an oscillatory bifurcation that only preserves R_2 symmetry. The sign of the real part of the most representative eigenvalues is included; the parenthesis denotes a complex eigenvalue. $\Gamma = 2$.

C. Basic flows and stability σ = [0.02492 − 0.026]

To describe the bifurcation scenario for $0.02492 \leq \sigma \leq 0.026$ we show in Fig. 11 the value of E_0 (contribution of zero-azimuthal modes to the mean value of the kinetic energy) of G symmetric steady solutions as a function of the Rayleigh number for different values of the Prandtl number in this range. For $\sigma = 0.02492$ (Fig. 11(a)) we have obtained two branches of solutions. The branch on the left (almost a straight line) extends to lower values of the Rayleigh number and corresponds to the basic flow previously described. The solutions of this branch are stable until $Ra = 1.279 \times 10^4$ (open circle), where a stationary instability maintaining R_1 occurs. The solutions in the upper part of the second branch, those in the zone that extends to higher values of the Rayleigh number, are unstable with two positive real eigenvalues, one corresponding to an eigenvector preserving the G symmetry and the other the R_1 symmetry. It is worth remarking that we have continued numerically the branch on the left and the upper part of the second branch as far as $Ra = 2.1 \times 10^4$ and they still keep separate. By decreasing the value of the Rayleigh number in the upper part of the second branch, a bifurcation that preserves the R_1 symmetry of the solution takes place at $Ra = 1.366 \times 10^4$ (open circle). For lower values of the Rayleigh number, the solutions in the upper part of the second branch remain still unstable but with only one positive real eigenvalue, corresponding to an eigenvector preserving the G symmetry. At the saddle-node $Ra = 9923$, the solutions in the lower part of the second branch gain stability. When the Rayleigh number is increased through the lower part of the second branch, a new bifurcation, now of oscillatory nature ($\omega = 21.0$) and that preserves the R_2 symmetry, takes place at $Ra = 1.301 \times 10^4$ (filled circle in Fig. 11). From this point, the solutions of the lower branch are unstable. To help the reader, we have included in Fig. 11 the sign of the real part of the most representative eigenvalues, the parenthesis indicating the complex eigenvalue that preserves the R_2 symmetry. Thus, there is a region in which two stable solutions preserving all the symmetries coexist. Both solutions look very similar, and it is not easy to distinguish them. To remark their differences we display in Fig. 12 the projections of the velocity field on the cross section $z = \Gamma/2$ and onto the horizontal plane L_h of the two stable G-symmetric steady solutions of $\sigma = 0.02492$ at the bifurcation points $Ra = 1.279 \times 10^4$ (left branch, straight line) and $Ra = 1.301 \times 10^4$ (lower part of the second branch).

The flow in Fig. 12(a) is of the same type as the basic flow described in Secs. II C–III A (Figs. 2 and 4), although it has undergone some transformations. For example, the four vortices near the horizontal line parallel to y-axis in the cross section at $z = \Gamma/2$, have become stronger and have moved away from this line, the stagnation points have displaced from the center and the radial velocity in this line compared to the values of the projection of the velocity in the same section has weakened. The maximum transverse velocity in this section $v_t = 2.6$ is on the vertical diameter. In the horizontal plane L_h the four vortices in the corners have widened and the maximum value of the projection of the velocity on the this plane is $v_h = 6.8$.

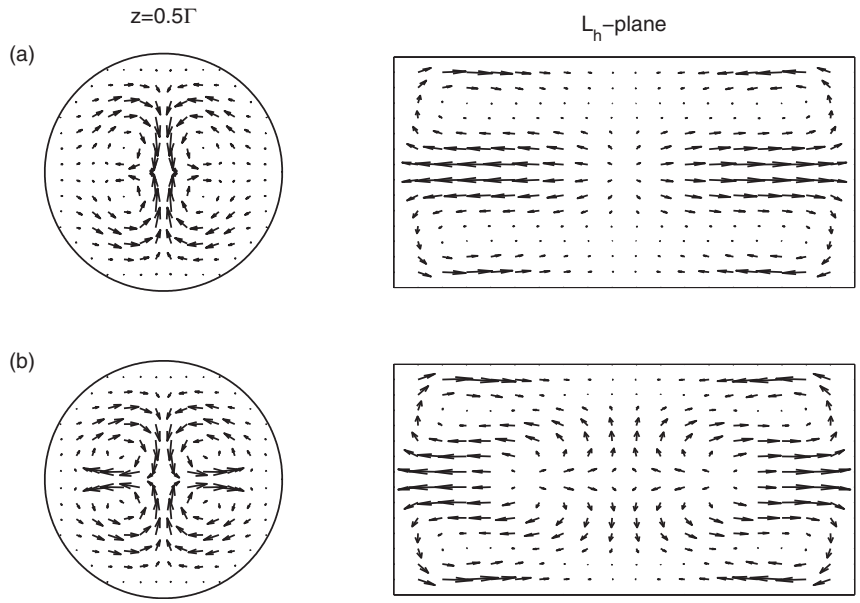

FIG. 12. Transverse velocity field in the vertical cross section $z = \Gamma/2$ and the projection of the velocity field onto the horizontal plane L_h for the G-symmetric steady solutions at the critical points (a) $Ra = 1.267 \times 10^4$ and (b) $Ra = 1.301 \times 10^4$ (see the text). $\sigma = 0.02492$, $\Gamma = 2$.

The solution in the new stable branch (Fig. 12(b)) is characterized by having, in the cross section at $z = \Gamma/2$, a stronger radial velocity near the horizontal line parallel to y-axis, directed from the center towards the lateral wall. The maximum transverse velocity $v_t = 2.7$ is now on the horizontal line. In the horizontal plane L_h, we observe that in the axis of the cylinder two stagnation points appear. The fluid flows from these points towards the lids and towards the center. The maximum value of the projection of the velocity on the horizontal plane is $v_h = 5.5$, a lower value in spite of having higher value of the Rayleigh number.

In Fig. 11(b) we can see for $\sigma = 0.025$ the transformation of the previous bifurcation diagram for $\sigma = 0.02492$. In between, a branching bifurcation that reconnects the branches takes place and the two bifurcation points of the instabilities that maintain R_1 (open circle) merge and this instability disappears in both disconnected branches. The disconnected upper branch moves up quickly when the Prandtl number increases. For $\sigma = 0.025$ the saddle-node is by $Ra = 1.363 \times 10^4$ and for $\sigma = 0.02525$ the saddle-node is by $Ra = 1.722 \times 10^4$. The solutions in the lower disconnected branch in the zone that extends to lower values of the Rayleigh number are stable until a saddle-node at $Ra = 1.125 \times 10^4$ is reached (in fact, there are three saddle-nodes very close). In this region, the real eigenvalue associated to the stationary instability that maintains R_1 symmetry is always negative; although it begins to approach to zero, right before the location of the saddle-node, it reaches its maximum value and becomes again more negative. At the saddle-node ($Ra = 9905$) the solutions become stable. By increasing the Rayleigh number there is a bifurcation at $Ra = 1.301 \times 10^4$, which is oscillatory and preserves the R_2 symmetry as in the $\sigma = 0.02492$ case. Again, there is a region where two stable solutions preserving all the symmetries coexist.

For $\sigma = 0.026$ this region of bistability no longer exists (see Fig. 11(c)) and the solutions are stable until $Ra = 1.396 \times 10^4$, where the oscillatory instability that preserves the R_2 symmetry occurs. Thus, a codimension-2 *cusp* bifurcation takes place between $\sigma = 0.025$ and $\sigma = 0.026$. The upper disconnected branch is out of scale.

To describe this instability, we display in Fig. 13(left) the real and imaginary parts of the temperature deviation of the dominant eigenvector in two cross sections at distances $z = \Gamma/4$, $3\Gamma/4$

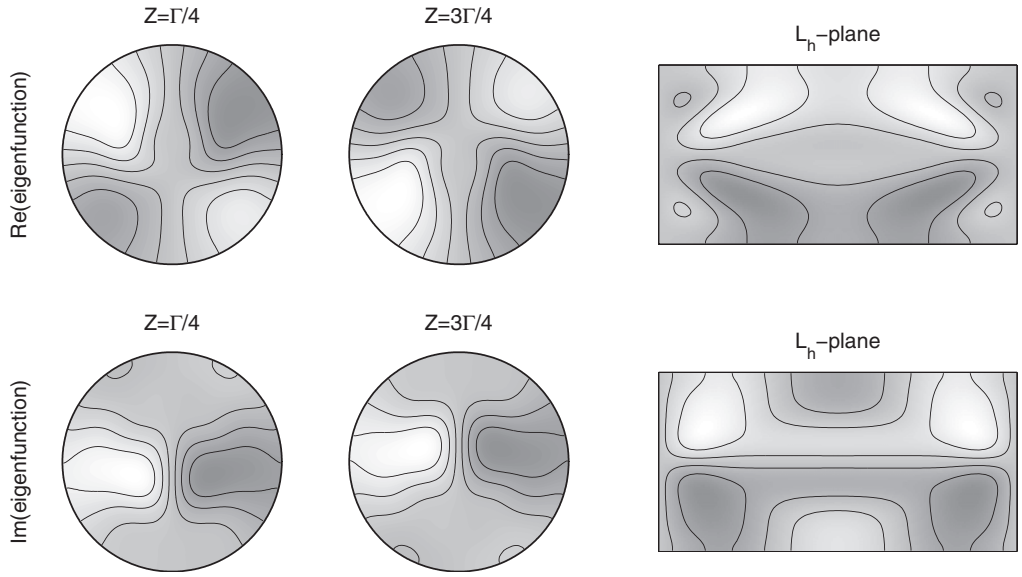

FIG. 13. Eigenvector responsible for the instability at the critical point $\sigma = 0.026$, $Ra = 1.396 \times 10^4$. The instability is oscillatory, preserves the R_2 symmetry of the basic flow and breaks the R_1 and R_3 symmetries. Real and imaginary part of the temperature deviation: (left) in two cross sections at distances $z = \Gamma/4, 3\Gamma/4$ of the hot lid, (right) in the horizontal plane L_h (the positive x-axis, perpendicular to the paper, points downwards). Gray-levels for cross sections and horizontal planes plots have different scales. $\Gamma = 2$.

of the hot lid for $Ra = 1.396 \times 10^4$ and $\sigma = 0.026$. The temperature deviation satisfies

$$\Theta(r, \theta, z) = -\Theta(r, -\theta, z), \qquad \text{i.e.,} \qquad R_1\Theta = -\Theta, \tag{21}$$

$$\Theta(r, \theta, \Gamma/4) = -\Theta(r, \theta + \pi, 3\Gamma/4), \qquad \text{i.e.,} \qquad R_2\Theta = +\Theta, \tag{22}$$

$$\Theta(r, \theta, \Gamma/4) = +\Theta(r, \pi - \theta, 3\Gamma/4), \qquad \text{i.e.,} \qquad R_3\Theta = -\Theta. \tag{23}$$

The antisymmetric nature with respect to R_1 and R_3 transformations can be appreciated in Fig. 13(right) where we display Θ in the horizontal plane ($\theta = \pi/2, -\pi/2$). Again, as a consequence of the breaking of symmetry R_1, the deviation of temperature is null in the vertical plane ($\theta = 0, \pi$). The production of the kinetic energy in this bifurcation comes also from the shear term (see Table I). The azimuthal structure of the eigenfunction is now dominated by the $n = 1$ and $n = 2$ modes and incorporates significant contributions of modes $n = 3$ and $n = 0$ (see Fig. 14).

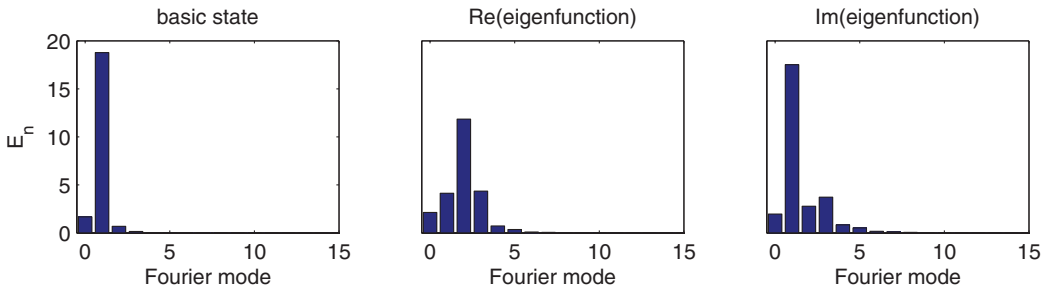

FIG. 14. Bar charts showing the azimuthal contribution E_n to the mean kinetic energy for the basic flow and for the real and imaginary parts of the critical mode at bifurcation points. $Ra = 1.396 \times 10^4$, $\sigma = 0.026$, $\Gamma = 2$.

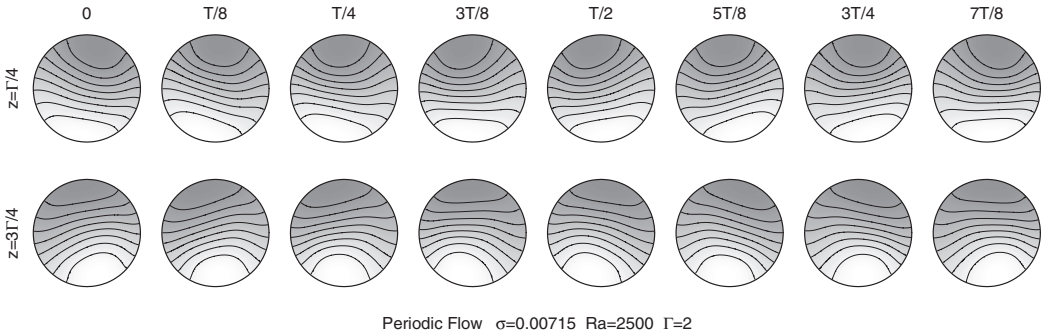

FIG. 15. Snapshots at equispaced time intervals that span a full period of two symmetrical cross sections perpendicular to the cylinder axis. The contour plots represent the deviation of the temperature field for $Ra = 2500$, $\sigma = 0.00715$, $\Gamma = 2$.

D. Secondary flows

In Secs. III B–III C we have analyzed in detail the stability of the basic flow and have identified four different modes of instability in the range of Prandtl numbers considered. Here we will describe the saturated states reached once the threshold of the instability is crossed for some selected values of the Prandtl number, one for each of the identified modes of instability shown in Fig. 6. In the four cases that have been studied, the bifurcations are supercritical. The procedure we follow consists in setting a slightly supercritical Rayleigh number for which the time dependent governing equations are numerically integrated until a secondary flow is reached. We take as initial condition the basic flow below onset. Below we describe in detail the saturated solutions in each of four different cases.

1. Oscillatory flow with R_1 and R_2 broken symmetries ($\sigma = 0.00715$, $Ra = 2500$)

For this value of the Prandtl number, the first instability of the basic flow is oscillatory. This is the case analyzed in Sec. III A, where the basic flow has been described in detail (Figs. 2, 3 and 4). The onset of instability is through a Hopf bifurcation that takes place at $R_c = 1.885 \times 10^3$, as computed in Sec. III A. The bifurcation breaks the symmetries R_1 and R_2 and only the symmetry R_3 is preserved. The flow also displays a space time symmetry such that the spatial action of R_1 and R_2 is exactly compensated by an evolution in time of half a period.

Fig. 15 represents the flow for a supercritical value of the Rayleigh number ($R = 2500$) in two symmetrical cross sections perpendicular to the cylinder axis. This is a convenient way to grasp the symmetries of the flow, as explained previously. Here we present eight snapshots of the deviation of the temperature field at cross sections perpendicular to the cylinder axis. The snapshots are presented at equispaced time intervals in one period ($T = 2.17$). From the figure we can appreciate that the temperature isosurfaces slosh inside the cylinder, and simultaneously there is a periodic variation of the temperature along the upper and lower intrusions of hot and cold fluid.

In Fig. 16 we represent the projection of the velocity field onto the L_h-plane at two different time instants separated half a period. It can be observed that the flow consists in four vortices; in each vortex the flow near the walls goes towards the central cross-section of the cylinder, and near the axis goes towards the lids of the cylinder, as in the basic flow. The difference in the flow between the two instantaneous flows displayed, is that the vortices become wider and narrower periodically in each side of the domain. As a consequence of the R_3 symmetry of the solution, this projection is reflection symmetric with respect to the vertical centerline of the rectangular plane L_h, as can be seen in the figure.

2. Symmetrical oscillatory flow ($\sigma = 0.014$, $Ra = 10000$)

In this case the bifurcation is oscillatory and preserves all the spatial symmetries, as the eigenfunction shows (Fig. 8) in Sec. III B. We have computed a saturated solution near the onset of the instability ($Ra_c = 9.967 \times 10^3$) and we have found the bifurcation to be supercritical. In this

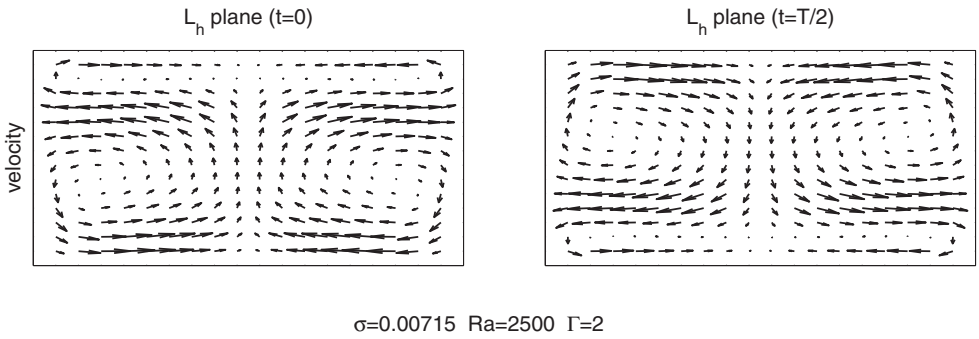

FIG. 16. Projection of the velocity field onto the horizontal plane L_h in two instants separated by a time interval of half a period. $Ra = 2500$, $\sigma = 0.00715$, $\Gamma = 2$.

region of the parameter space there are three modes crossing nearby, and the solution that first bifurcates remains stable in a small interval of Rayleigh numbers (this can be inferred from Fig. 6). In Fig. 17 we show the perturbation of the temperature field (we have subtracted the temporal averaged temperature field), for a saturated solution at a Rayleigh number $Ra = 10\,000$, which has a period $T = 0.72$. The figures represent eight snapshots at equispaced time intervals, of the temperature field at two different cross sections perpendicular to the cylinder axis at $z = \Gamma/4$ (top panels) and $z = 3\Gamma/4$ (bottom panels). It can be easily appreciated that all the symmetries are preserved at any time and that two snapshots a quarter of period apart match with the real and imaginary part of the eigenfunction in Fig. 8.

3. Stationary flow with R_2 and R_3 broken symmetries ($\sigma = 0.017$, $Ra = 1.030 \times 10^4$)

We have calculated a saturated steady flow for $\sigma = 0.017$ and $Ra = 1.030 \times 10^4$, slightly above the critical bifurcation point ($Ra_c = 1.005 \times 10^4$). In Fig. 18 velocity plots of the projection of the velocity and contour plots of the deviation of temperature on L_v and L_h planes are shown. In the plane L_v, the breaking of the reflection with respect to the center of the rectangle (a consequence of the breaking of R_2 and R_3 symmetries) is hardly noticed. However, in the L_h-plane, we notice clearly that the reflection symmetry with respect to the center of the rectangle is broken (as a consequence of the breaking of R_2 symmetry) and the same occurs with reflection through the vertical centerline of the plane (as a consequence of the breaking of R_3 symmetry). The flow keeps the R_1 symmetry, as can be seen in the figure from the symmetry of the reflection through the horizontal centerline in this plane (Fig. 18).

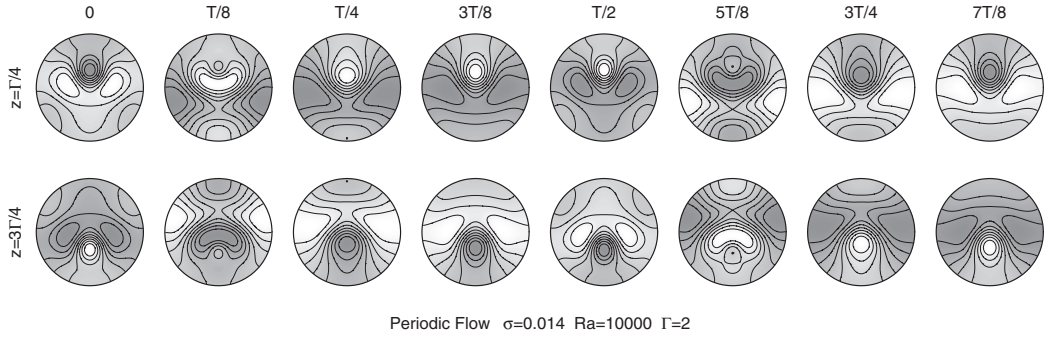

FIG. 17. Snapshots of the perturbation of temperature (we have subtracted the temporal averaged temperature field) at equispaced time intervals that span a full period. The top and bottom panels represent two symmetrical cross sections perpendicular to the cylinder axis at $z = \Gamma/4$ and $z = 3\Gamma/4$, respectively. $Ra = 10000$, $\sigma = 0.014$, $\Gamma = 2$.

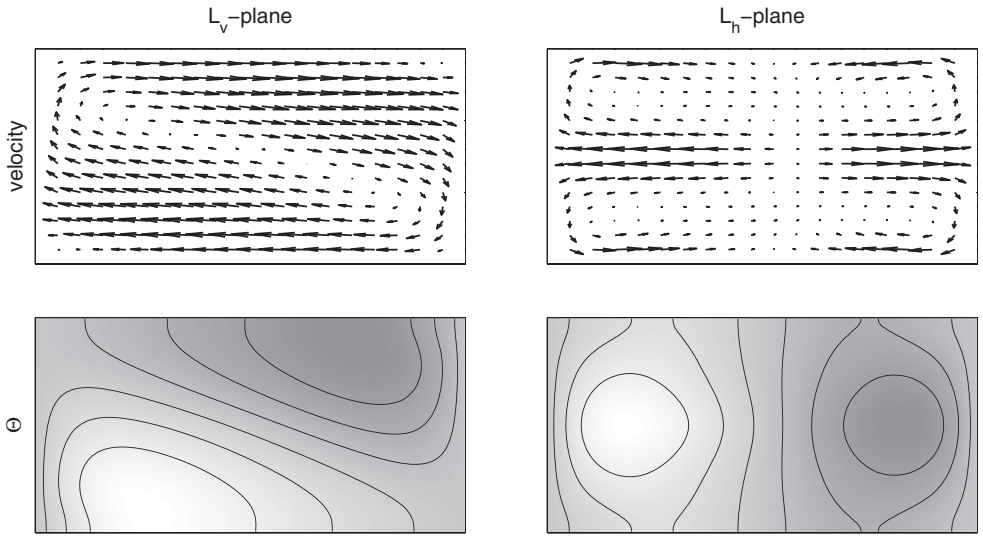

FIG. 18. Projection of the velocity field (top) and deviation of the temperature (bottom) on the vertical L_v plane, with the positive y-axis, perpendicular to the paper, pointing downwards (left panels), and on the horizontal L_h plane with the positive x-axis, perpendicular to the paper pointing downwards (right panels). $Ra = 1.030 \times 10^4$, $\sigma = 0.017$, $\Gamma = 2$.

4. Oscillatory flow with R_1 and R_3 broken symmetries ($\sigma = 0.026$, $Ra = 1.450 \times 10^4$)

For $\sigma = 0.026$ the first instability identified as the Rayleigh number is increased is oscillatory and breaks the R_1 and R_3 symmetries. For this value of the Prandtl number there is a single basic steady state that loses stability straight in a supercritical Hopf bifurcation at a value of the Rayleigh number around 1.396×10^4. We have obtained a saturated oscillatory solution for $Ra = 1.450 \times 10^4$ with a period $T = 0.28$. Fig. 19 represents, for this saturated solution, the projected velocity fields onto horizontal L_h plane at two different time instants half a period apart. It can be seen that the flow near the midplane vertical line (with respect to the figure) reverses direction every half a period and that the vortices located near the corner, now symmetric with respect to the center (R_2 symmetry is preserved), become wider and narrower periodically. Since this solution is obtained very near criticality, the deviation from the basic state is very small; however, the breaking of the reflection with respect the vertical and horizontal centerlines of the rectangular planes in Fig. 19 (as a consequence of the breaking of R_3 and R_1 symmetries) is clearly appreciated.

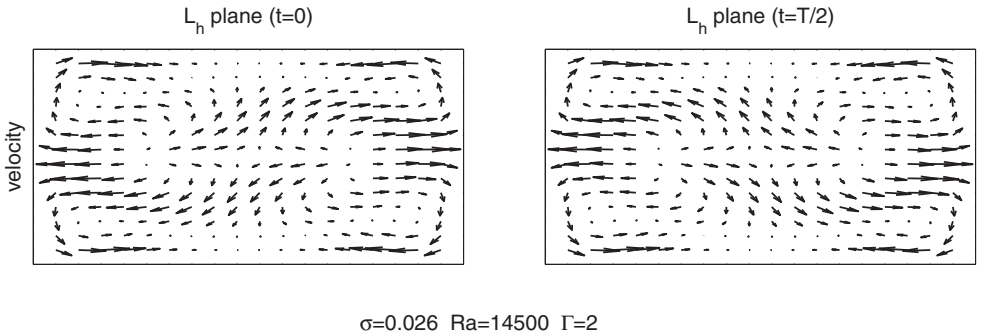

FIG. 19. Projection of the velocity field onto the horizontal plane L_h in two instants separated by a time interval of half a period. The positive x-axis, perpendicular to the paper points downwards. $Ra = 1.450 \times 10^4$, $\sigma = 0.026$, $\Gamma = 2$.

IV. CONCLUSIONS

In this paper we have studied the flow induced by an axial temperature gradient in a horizontal closed cylinder of aspect ratio $\Gamma = 2$, for a range of Prandtl numbers up to $\sigma = 0.026$, characteristic of molten metals at high temperature. The system models the melt zone in a horizontal Bridgman crystal growth method. In the system we consider, a pure conductive state is not allowed by equations and boundary conditions, and a fluid motion is always present, no matter how small the temperature gradient is. Due to the confined geometry, the basic flow, which displays all the symmetries of the equations and the applied boundary conditions, is strongly three dimensional. The main focus of this work has been to characterize the instability modes of this basic flow when the temperature gradient increases.

We have calculated the basic flow that develops in the system once a temperature gradient has been established. We have done the computations either by integrating the equations in time, until a steady state is settled, or by finding a steady solution using Newton's method. We have used a continuation algorithm to follow the branches of solutions and have calculated the leading eigenvalues along the branch to determine the instability threshold. The main results are summarized in Fig. 6, where the critical values are displayed for the full range of Prandtl numbers studied.

In the range of Prandtl numbers from zero to $\sigma = 0.026$, we have identified four different regions with instabilities which break different symmetries and are either oscillatory or stationary. We have also tried to elucidate if the instability mechanism is dominated by buoyancy or shear forces; from an energy analysis of the dominant eigenfunctions, we can conclude that the instability is dominated by shear, and that there are not significant differences in the shear contribution of the four modes encountered. The azimuthal contribution to the mean kinetic energy for each eigenvector shows some differences in their spectral decomposition; the steady bifurcation is dominated by the zero azimuthal mode whereas the oscillatory modes have significant contributions of the one and two azimuthal modes. In all cases the basic state displays the same spectra. We have characterized the structure of the flow resulting from these instabilities in order to gain additional insight on the physical mechanisms leading to them.

A similar study has been performed in a confined rectangular geometry (cross-section 2×1, and length 4) by Henry and BenHadid.[15] The authors find for very small Prandtl numbers a crossing from an oscillatory mode dominant in the region $0 \leq \sigma \approx 10^{-4}$, which maintains the symmetry equivalent to R_2, to a steady mode maintaining the symmetry equivalent to R_1, which dominates up to $\sigma \approx 0.015$. This behavior differs from what we have found in our system, where an oscillatory mode maintaining R_3 dominates up to $\sigma < 0.0132$ (see Ref. 6). For higher values of the Prandtl number, while in the rectangular cavity the dominant instability is oscillatory in the range $0.015 \leq \sigma \leq 0.025$ and maintains the symmetry equivalent to R_3, in our cylindrical cavity the secondary flow is steady and maintains R_1. The difference between these results shows that the geometry and the Prandtl number both have a dramatic influence in the instability of the basic flow, and in the oscillatory character of the instability.

Another important conclusion from our study is the supercritical character of all the instabilities, although the symmetric secondary periodic solution around $\sigma = 0.014$ is observed to be stable in a very narrow interval of Rayleigh numbers due to the presence of other unstable modes near threshold. Probably the modes will interchange stability when varying slightly the aspect ratio and we expect to see complex dynamics organized around these mode crossings.

In the vicinity of $\sigma = 0.025$ two different basic steady states with the same symmetry coexist for the same parameter values; the two states belong to the same solution branch, which has undergone a saddle-node bifurcation. This behavior seems to originate from a cusp bifurcation at a certain point in the parameter space (σ, Ra) and appears to be located near $\sigma \sim 0.026$. In the vicinity of this point the scenario is further complicated by the presence of a branching bifurcation near $\sigma = 0.02492$ (see Fig. 11(a)), pointing to a much richer solution phase-space than previously anticipated. The influence and relevance of this bifurcation scenario into the dynamics of the system remains to be seen and would merit further study.

The coexistence of two similar basic steady states has been also observed in rectangular geometry (Henry, private communication).

ACKNOWLEDGMENTS

The authors wish to thank Professor D. Henry and Dr. Arantxa Alonso for useful discussions and comments. This work is funded by DGICYT under Grant No. FIS2009-08821. O. Sanchez was supported by a FI grant from the DGR of the Generalitat de Catalunya.

[1] D. T. J. Hurle, E. Jackeman, and C. P. Johnson, "Convective temperature oscillations in molten gallium," J. Fluid Mech. **64**, 565–576 (1974).
[2] A. Y. Gelfgat, P. Z. Bar-Yoseph, and A. L. Yarin, "On oscillatory instability of convective flows at low Prandtl number," J. Fluids Eng. **119**, 823–830 (1997).
[3] I. Mercader, O. Batiste, and X. Ruiz, "Quasi-periodicity and chaos in a differentially heated cavity," Theor. Comput. Fluid Dyn. **18**(2-4), 221–229 (2004).
[4] J. E. Hart, "Stability of thin non-rotating Hadley circulations," J. Atmos. Sci. **29**, 687 (1972).
[5] P. Laure and B. Roux, "Linear and non-linear analysis of the Hadley circulation," J. Cryst. Growth **97**, 226–234 (1989).
[6] T. P. Lyubimova, D. V. Lyubimov, V. A. Morozov, R. V. Scuridin, H. Ben Hadid, and D. Henry, "Stability of convection in a horizontal channel subjected to a longitudinal temperature gradient. Part 1. Effect of aspect ratio and Prandtl number," J. Fluid Mech. **635**, 275–295 (2009).
[7] D. V. Lyubimov, A. V. Burnysheva, H. Ben Hadid, T. P. Lyubimova, and D. Henry, "Rotating magnetic field effect on convection and its stability in a horizontal cylinder subjected to a longitudinal temperature gradient," J. Fluid Mech. **664**, 108–137 (2010).
[8] M. Lappa, "Secondary and oscillatory gravitational instabilities in canonical three-dimensional models of crystal growth from the melt. Part 2: Lateral heating and the Hadley circulation," C. R. Mecanique **335**, 261–268 (2007).
[9] A. Y. Gelfgat, P. Z. Bar-Yoseph, and A. L. Yarin, "Stability of multiple steady states of convection in laterally heated cavities," J. Fluid Mech. **388**, 315–334 (1999).
[10] I. Mercader, O. Batiste, L. Ramírez de la Piscina, X. Ruíz, S. Rüdiger, and J. Casademunt, "Bifurcations and chaos in single-roll natural convection with low Prandtl number," Phys. Fluids **17**, 104108 (2005).
[11] M. A. Christon, P. M. Gresho, and S. B. Sutton, "Computational predictability of time-dependent natural convection flows in enclosures (including benchmark solution)," Int. J. Numer. Meth. Fluids **40**, 953–980 (2002).
[12] A. Y. Gelfgat, "Stability and slightly supercritical oscillatory regimes of natural convection in a 8:1 cavity: solution of the benchmark problem by a global Galerkin method," Int. J. Numer. Methods Fluids **44**, 135–146 (2004).
[13] R. J. A. Janssen and R. A. W. M. Henkes, "Instabilities in three-dimensional differentially-heated cavities with adiabatic horizontal walls," Phys. Fluids **8**, 62 (1996).
[14] A. Y. Gelfgat and S. Molokov, "Quasi-two dimensional convection in a three-dimensional laterally heated box in a strong magnetic field normal to main circulation," Phys. Fluids **23**, 034101 (2011).
[15] D. Henry and H. BenHadid, "Multiple flow transitions in a box heated from the side in low-Prandtl-number fluids," Phys. Rev. E **76**, 016314 (2007).
[16] B. Hof, A. Juel, L. Zhao, D. Henry, H. Ben Hadid, and T. Mullin, "On the onset of oscillatory convection in molten Gallium," J. Fluid Mech. **515**, 391 (2004).
[17] A. Juel, T. Mullin, H. Ben Hadid, and D. Henry, "Three-dimensional free convection in molten Gallium," J. Fluid Mech. **436**, 267 (2001).
[18] S. Vaux, H. Ben Hadid, and D. Henry, "Study of the hydrodynamic instabilities in a differentially heated horizontal circular cylinder corresponding to a Bridgman growth configuration," J. Cryst. Growth **290**, 674–682 (2006).
[19] I. Mercader, O. Batiste, and A. Alonso, "An efficient spectral code for incompressible flows in cylindrical geometries," Comput. Fluids **39**, 215–224 (2010).
[20] S. Hugues and A. Randriamampianina, "An improved projection scheme applied to pseudospectral methods for the incompressible Navier-Stokes equations," Int. J. Numer. Methods Fluids **28**, 501–521 (1998).
[21] B. Fornberg, *A Practical Guide to Pseudospectral Methods* (Cambridge University Press, Cambridge, 1998).
[22] L. N. Trefethen, *Spectral Methods in Matlab* (SIAM, Philadelphia, 2000).
[23] I. Mercader, M. Net, and A. Falqués, "Spectral methods for high order equations," Comput. Methods Appl. Mech. Eng. **91**, 1245–1251 (1991).
[24] I. Mercader, A. Alonso, and O. Batiste, "Spatiotemporal dynamics near the onset of convection for binary mixtures in cylindrical containers," Phys. Rev. E **77**, 036313 (2008).
[25] F. Marqués, I. Mercader, O. Batiste, and J. López, "Centrifugal effects in rotating convection: Axisymmetric states and three-dimensional instabilities," J. Fluid Mech. **580**, 303–318 (2007).
[26] J. López, F. Marqués, I. Mercader, and O. Batiste, "Onset of convection in a moderate aspect-ratio rotating cylinder: Eckhaus-Benjamin-Feir instability," J. Fluid Mech. **590**, 187–208 (2007).
[27] C. K. Mamun and L. S. Tuckerman, "Asymmetry and Hopf bifurcation in spherical Couette flow," Phys. Fluids **7**, 80–91 (1995).
[28] V. Frayssé, L. Giraud, S. Gratton, and J. Langou, "A set of GMRES routines for real and complex arithmetics on high performance computers," Technical Report No. TR/PA/03/3, CERFACS; Public domain software available on www.cerfacs/algor/Softs (2003).
[29] A. Bergeon and E. Knobloch, "Natural doubly diffusive convection in three-dimensional enclosures," Phys. Fluids **14**(9), 3233–3250 (2002).
[30] D. Ma, D. Henry, and H. BenHadid, "Three-dimensional numerical study of natural convection in vertical cylinders partially heated from the side," Phys. Fluids **17**, 124101 (2005).